Chapter 1

Introduction

1.1   A brief history on the search for exoplanets

Pondering on the existence of worlds other than our own has always piqued human interest. There have been centuries of speculation on whether our planet, the Earth, and our planetary system, the Solar System, were ones of many. As early as the 3rd century B.C., Epicurus (341-270 B.C.) said *"There are infinite worlds both like and unlike this world of ours. For the atoms being infinite in number, as was already proven, (...) there nowhere exists an obstacle to the infinite number of worlds"*. But his point of view was not commonly shared, as for instance by the philosopher Aristotle (384-322 B.C.) who claimed *"There cannot be more worlds than one"*. It was only in 1609 that Galileo Galilei (1564-1642) first observed with a telescope other planets in our Solar System, confirming the idea of Copernicus (1473-1543) that the sun is orbited by several planets, of which the earth is but one.

Our search for other worlds, need not to be limited to our Solar System. Indeed, the search for exoplanets, planets around other stars than the Sun, has already begun. However, unlike the planets in our Solar System which are close to us and thus appear very bright, exoplanets are very difficult to observe directly. The light of a planet is millions of times fainter than the light of its star. When seen from tens to thousands of light years[1] away, the planet appears very close to its star and its faint light is diluted in the glare of its star. Indirect methods designed to detect an exoplanet through its influence on its parent star or on other field stars, avoid these difficulties of contrast, and so have become successful and popular methods for detecting exoplanets. These methods by which exoplanets have been detected are briefly described in Section 1.2.1.

Several claims of exoplanet detections have been documented since the 19th century, but the first confirmed detections were made by Wolszczan & Frail (1992) who monitored the irregularities in the timing of pulsars. These exoplanets, PSR 1257+12 b and c, are a few Earth masses and orbit a pulsar[2] at radii similar to that at which Mer-

---

[1] A light year is the distance covered when travelling at the speed of light over one year.

[2] A pulsar is a very dense star, resulting from the collapse of the core a massive star during a supernovae,

cury orbits the Sun. The first discovery of an exoplanet around a star similar to the Sun was made by monitoring variations in the radial velocity of a star (Mayor & Queloz, 1995). This exoplanet, 51 Pegasi b, is classified as a Hot Jupiter as it is similar in mass to Jupiter (half the mass) and it orbits close to its star (about 8 times closer than Mercury orbits the Sun). The discovery of Hot Jupiters challenged our understanding of planet formation and evolution. Gas giant planets were originally expected to form beyond the snow line[3] and so were expected to be found at orbits similar to those of the giant planets in our Solar System (Pollack et al., 1996). But finding them so close to their stars prompted people to suggest that these planets may have undergone inward migration after their formation, due to interactions with their parent protoplanetary discs (Lin et al., 1996).

In the past two decades, the number of exoplanets discovered has gone from zero to more than 400. This progress is the result of several improvements in instrumentation and observing techniques, such as the development of CCD[4] cameras, the development of stable high resolution spectroscopy, and the introduction of computer-based image processing. It is also the result of an increased interest in the field of exoplanets and in the diversification of the techniques used to detect exoplanets.

In the 1950s, the first papers on the search for exoplanets using the transit method were published (e.g. Struve 1952), and the first detailed development of this detection method was carried out shortly after (Rosenblatt, 1971). The first observation of the transit of an exoplanet was published in Charbonneau et al. (2000). This planet, HD 209458b, was first discovered with the radial velocity technique (Mazeh et al., 2000). The combined detection of the planet's transit and radial velocity effect on its parent star opened a new area in the study of exoplanets, this combination of technique allows both the planet's radius and mass to be measured. These can then be compared to the predictions of planet evolution models with various compositions and heat deposition mechanisms (e.g. Guillot 2005, Baraffe et al. 2008) to infer the planet's bulk composition. These models are continuously challenged by new planet discoveries, the best known case of this being the small group of planets whose radii are larger than expected for their mass and irradiation level: HD 209458b (Charbonneau et al., 2000; Knutson et al., 2007b), HAT-P-1b (Bakos et al., 2007; Winn et al., 2007), WASP-1b (Collier Cameron et al., 2007; Charbonneau et al., 2007), TrES-4b (Mandushev et al., 2007), XO-3b (Winn et al., 2008), CoRoT-2b (Alonso et al., 2008), and WASP-12b (Hebb et al., 2009). To explain the inflated radii of these planets, most models require an additional heating mechanism that deposits energy deep into the atmosphere of the planet.

To date (March 2010), 431 exoplanets[5] have been discovered, more than 80 are

---

rotating around itself very rapidly and emitting very regular polar electromagnetic pulses.

[3]The snow line is the distance from the protostar where the temperature is low enough for the hydrogen compounds in the solar nebulae (e.g. water, ammonia, methane) to condense into ice grains.

[4]CCD stands for Charged Coupled Device

[5]http://exoplanet.eu/catalog.php

in multiple planet systems, more than 400 have been observed through radial velocity measurements, the transits of 70 of them have been observed, and at least 4 exoplanets[6] have been imaged directly.

1.2   The detection of exoplanets

1.2.1   The methods

There are several methods that have successfully detected exoplanets, and several other proposed methods which have not yet detected an exoplanet. Perryman (2000) and Lunine et al. (2008) review the different techniques and their performance and limitations. In this thesis, I focus on the science and usage of the transit method and use some information from the radial velocity method. I describe these two methods hereafter. For completeness I also describe in this section the other methods that have successfully detected one or more exoplanets to date. A summary of the different parameters measurable from the different methods is presented in Table 1.1.

The transit method

This method detects the passage of a planet in front of its host star. This event is called a *transit*. The passage of the planet behind its host star is called an *occultation* or a secondary eclipse. Jupiter creates a transit of 1% depth in front of the Sun, and the Earth create a depth of 0.08%. The observation of the transit of a planet allows one to derive the dimensions of the planet relative to its host star, the planet to star separation, and the orientation of the planet's orbit relative to the plane of the sky, as described in Section 1.3.1. For a transiting object to be confirmed as a planet, its mass needs to be measured through the radial velocity follow-up of its parent star. For a transit to occur, the exoplanetary system needs to be seen nearly edge-on, which reduces the probability of a transit detection. The transit method is most sensitive to close-in planets as the probability of observing their transits is higher. The lower limit of detectable planet size depends on the photometric precision of the light curve. To increase the probability of transit detections within a survey, thousands of stars need to be monitored continuously with high precision photometry. The basic geometry and physics of transits is reviewed in Winn (2010).

The radial velocity method

This method detects the oscillating Doppler shift in the stellar spectrum due to the periodic radial velocity motion (motion along the line of sight) of a star gravitationally

---

[6]This number depends on the definition of an exoplanet. To date (March 2010), there are 4 exoplanets with $M_\mathrm{p} < 13 M_\mathrm{Jup}$ (above is the brown dwarf regime) orbiting a star (spectral class above M6; below is the brown dwarf regime).

tugged back and forth by an orbiting planet. For instance, Jupiter induces a radial velocity variation on the Sun of $12.5\,\mathrm{ms}^{-1}$, and the Earth a radial velocity variation of $0.1\,\mathrm{ms}^{-1}$. A close-in Jupiter-like exoplanet, such as 51 Pegasi b, induces a radial velocity variation on its host star of about $50\,\mathrm{ms}^{-1}$. The mass of a planet ($M_\mathrm{p}\sin i$, with i the inclination of the planet orbital plane to the plane of the sky) can be measured from the amplitude of the radial velocity variation it causes on its host star (see Section 1.3.2 for formulae). For the true mass to be measured, the inclination angle, i is needed, which can be obtained from transit observations if the planet transits its host star. The radial velocity method is most sensitive when the system is seen edge-on as the radial gravitational tug then appears stronger.

The microlensing method

This method detects the magnification of the light of a background star due to the deflection of its light by the gravitational field of a foreground star and its planet acting as a gravitational lens. The foreground star acts as the main lens and the orbiting planet is a much more short lived lens that acts in addition to the lensing of its host star. The magnification of the background light lasts for $\sim$100 days for the host star, and the superimposed magnification due to the planet lasts for $\sim$2 h for a Jupiter-size planet. The microlensing technique is sensitive to exoplanets down to Earth-sizes. The detection of small planets depends on the time sampling as the smaller the planet, the shorter the microlensing event. The sensitivity of the microlensing technique peaks for planet to star separations equal to the Einstein radius, typically corresponding to a separation just beyond the snow line. This technique requires a crowed stellar background so microlensing surveys are performed along the Galactic disk. The theory of the microlensing method applied to exoplanets is reviewed in Gaudi (2010).

The pulsar timing method

This method detects periodic anomalies in the frequency of the radio pulse of a neutron star, a remnant of super-novae. An Earth-like planet around a pulsar creates a detectable pulse delay of 1.2 miliseconds. This method is limited to pulsars.

The direct imaging method

This method detects the light of a planet itself (emitted or reflected from the star), and works for those planets that are far enough from their parent stars such that the stellar glare can be suppressed. The suppression of the stellar light can be done using an occulter – a chronograph – to block the light from the star, or an interferometer to nullify it. In optical wavelenghts Jupiter is 10^9 times less luminous than the Sun, and the Earth is ten times fainter than Jupiter. In the mid-infrared, the Earth is 10^6 times fainter than the

Sun. The direct imaging technique uses adaptive optics to sharpen the image of the star which is then easier to suppress, and to sharpen the image of the planet which is then easier to detect.

1.2.2   Properties of the exoplanets discovered to date

Figure 1.1 displays the ranges in planet mass, radius and orbital distance of the exoplanets detected by Jan 26th 2010, for each of the detection methods mentioned in section 1.2.1.
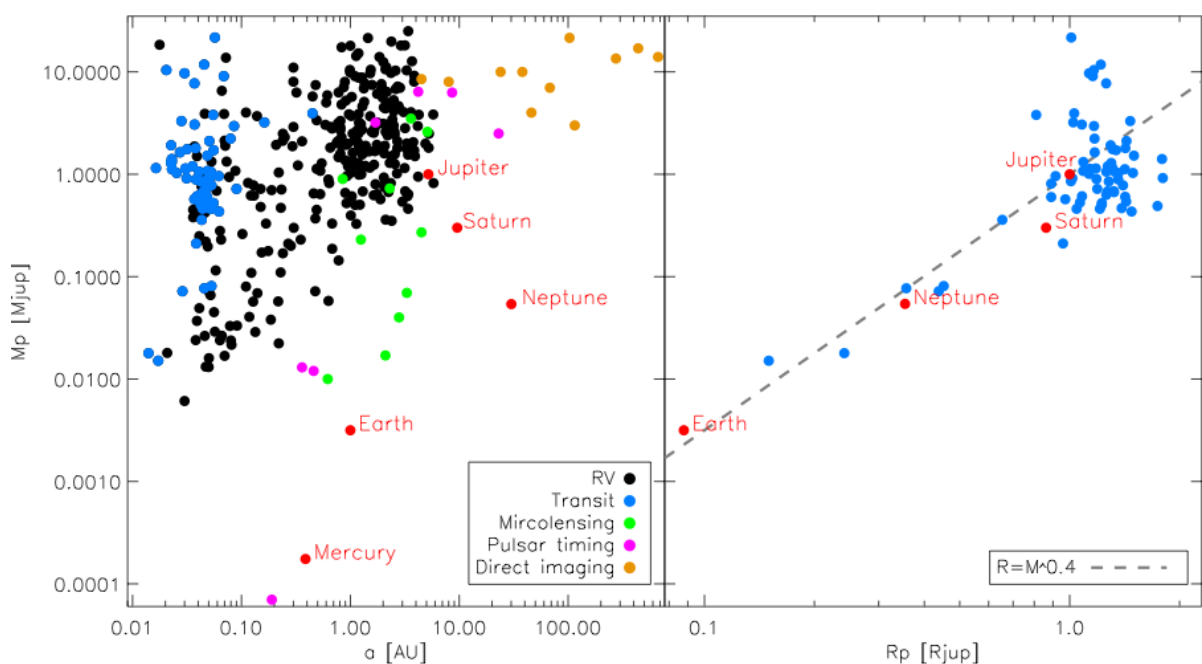
Figure 1.1: Graph of the masses, radii and orbital distances of the exoplanets detected by Jan 26th 2010, with the detection methods marked in different colours. The planet masses indicated for the radial velocity method (RV) are the lower limits of their $M_p \sin i$ value. The grey dash line (right panel) shows the mass-radius relation for $R_p = M_p^{0.4}$.

Some features in the distribution of the detected exoplanets stand out in Figure 1.1. The transiting planets are detected at small orbital distances from their host stars (≤ 0.5 AU so far); this is a bias of the transit method as close-in planets have a larger probability to transit. The planets detected by direct imaging have larger orbital distances (≥ 4 AU so far); this is due to the current performance of the stellar nulling techniques which detect planets more easily when they are well outside the residual stellar glare. Most of the exoplanets detected by radial velocity measurements have masses and radii similar to, or larger than Jupiter; this is because the perturbations caused by massive planets on their host stars are larger, making these planets easier to detect. The pulsar timing method allows the detection of very small planets, smaller than Mercury. The

transit, radial velocity and microlensing techniques have so far allowed the detection of planets down to a few times the size or mass of the Earth. As the instrumental technology and the data analysis techniques evolve and as the on-going surveys monitor the stars for longer, these observational biases should reduce.

Exoplanets are found with eccentricities ranging from 0 to 0.97, while in our Solar System the maximum planet orbital eccentricity is 0.2 (Mercury). Planet-planet and planet-star interactions can induce larger orbital eccentricities and inclinations to the stellar rotation plane.

The sky-projected planet orbital inclination and the sky-projected inclination between the stellar spin and the planet's orbit rotation axis, have been measured for some exoplanets. With the latter, polar or retrograde planet orbits can be identified. However, as the inclinations are degenerate over the inclination to the plane of the sky, it is not possible to compare them to the values in the Solar System or in the planet formation and evolution models.

So far, the exoplanet search surveys have been focussed on solar-type stars (F,G,K stellar type) and small stars, especially the radial velocity and transit surveys for which planets give larger amplitude signatures on smaller stars. This is a bias that will be adjusted with surveys on massive stars (larger than a few solar masses).

Solar-type stars harbouring giant exoplanets have been found to have a higher metallicity than the Sun (e.g. Santos et al. 2004). However, the observed population of planets around different mass and different metallicity stars is too small to give robust statistics. Currently, it is not possible to obtain reliable trends in how the number of planets varies with these stellar properties.

Table 1.1: Table of the planet parameters and the stellar parameters relevant to deriving them, Plus the associated observable(s) and observing method(s) used to derive the physical parameters.

Parameters	Observables	Method	Ref.
Planet			
Orbital period P	time of transits	light curve - transit	(1)
Orbital inclination i [1]	t_F, t_T, δ, P	light curve - transit	(1)
Planetary radius [2] $(R_{\rm p}/R_\star)$	δ	light curve - transit	(1)
Planetary mass [3] $((M_{\rm p}\sin i)/(M_{\rm p}+M_\star)^{2/3})$	$K_\star$	radial velocity curve	(2)
$(M_p/M_\star)$	shape of magn.	mircolensing	(3)
$(M_p \sin i)$	pulse delay	pulsar timing	(4)
Orbital semi-major axis $(a/R_\star)$	t_F, t_T, δ, P	light curve - transit	(1)
$(a \sin i)$	$K_\star$	radial velocity curve	(2)
$(a \sin i)$	t_m	microlensing	(3)
$(a \sin i)$	pulse delay	pulsar timing	(4)
$(a \sin i)$	α_p, d	direct imaging	(5)
Orbital eccentricity e	ϕ_{sec}	light curve - occultation	(6)
	RV shape	radial velocity curve	(2)
Argument of periastron ω	RV shape	radial velocity curve	(2)
Absorption spectrum	δ at various λ	light curve - transit	(1)
Emission spectrum	δ_{sec} at various λ	light curve - occultation	(6)
	$L_{\rm p}/L_\star$ at various λ	direct imaging	(5)
Thermal emission	δ_{sec} (large λ)	light curve - occultation	(6)
Albedo	δ_{sec} (small λ)	light curve - occultation	(6)
Phase function	flux ampl., ϕ_{max}	light curve - orbit	(7)
Planetary wind speed	ϕ_{max}	light curve - orbit	(7)
Spin-orbit angle λ_p [4]	shape of rossiter	radial velocity - transit [5]	(8)
Stellar spin angle [6]	oscill. modes	asteroseismology	(9)
Star			
Stellar mass $M_\star$	$T_{\rm eff}, \log g, [M/H]$	stellar evolution models	(10)
Stellar radius $R_\star$	$T_{\rm eff}, \log g, [M/H]$	stellar evolution models	(10)
	oscill. modes	asteroseismology	(9)
Stellar density $(M_\star/R_\star^3)$	t_F, t_T, δ, P	light curve - transit	(1)
	oscill. modes	asteroseismology	(9)
Limb darkening	transit shape	light curve - transit	(1)
Stellar rotation period	period of spots	light curve - stellar spots	(11)
Stellar age	rotation period	light curve - stellar spots	(11)
	$T_{\rm eff}, \log g, [M/H]$	stellar evolution models	(10)

Notations: t_F is the transit duration with the planet disk fully superimposed to the stellar disk, t_T is the total transit duration, δ is the transit depth, $K_\star$ is the semi-amplitude of the stellar radial velocity variation due to the planet, magn. stands for magnification, a is the planet orbital semi-major axis, d is the distance of the star to the Sun, ampl. stands for amplitude of the deviation, t_m is the time difference between the magnification maximum due to the star and the one due to the planet, α_p is the angular distance between the planet and the star, ϕ_{sec} is the phase in the planet orbit of the mid-occultation relative to the phase of the mid-transit, RV stands for radial velocity, λ is the wavelength, δ_{sec} is the depth of the occultation, $L_p/L_\star$ is the planet-to-star luminosity ratio, ϕ_{max} is the phase of the maximum flux in the planet orbit, oscill. stands for stellar oscillation, $T_{\rm eff}$ is the stellar effective temperature, g is the surface gravity, (M/H) is the metallicity of the star relative to the solar metallicity.

Notes: [1] projected onto the plane of the sky, [2] relative to the radius of the host star, [3] relative to the mass of the host star, [4] angle between the stellar spin axis and the perpendicular to the planet orbital plane, projected onto the plane of the sky, [5] Rossiter-McLaughlin effect, perturbation over the radial velocity curve during the planet transit, [6] angle between the stellar spin axis and the plane of the sky.

Example of reference: (1) Charbonneau et al. 2000, (2) Mazeh et al. 2000, (3) Bennett 2009, (4) Phillips & Thorsett 1994, (5) Marois et al. 2008, (6) Charbonneau et al. 2005, (7) Knutson et al. 2007a, (8) Gaudi & Winn 2007, (9) Kjeldsen et al. 2009, (10) Torres et al. 2009, (11) Aigrain et al. 2008.

1.3   Characterising exoplanets

The different detection methods allow the measurement of different planet param-
eters, as summarised in Table 1.1. The planet properties measurable from the planet
transit light curve and from the stellar radial velocity curve are described in sections
1.3.1, 1.3.2 and 1.3.3. The main properties of the exoplanets detected to date, and
of their host stars are listed in section 1.2.2. More detailed descriptions of the physi-
cal properties of the detected exoplanets and of their environment can be found in
Perryman (2000) and Baraffe et al. (2010).

1.3.1   Analytic equations to derive the planet parameters from the transit light curve

Equations for a uniform intensity stellar disk and a planet in circular orbit
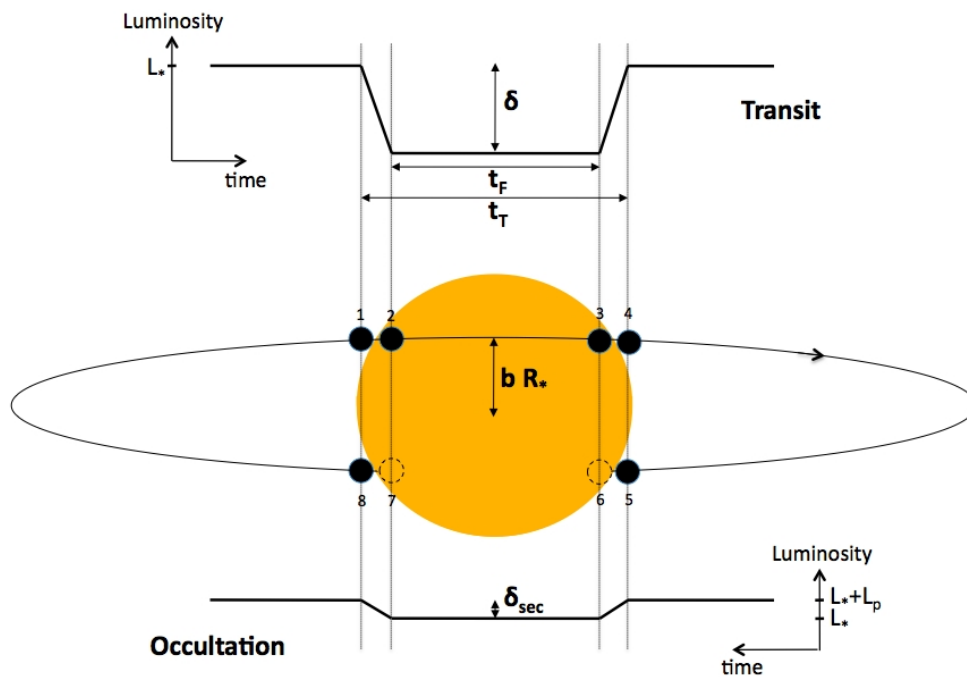

Figure 1.2: The schematic of a planet transiting its host star (middle) with the corre-
sponding variation in brightness during the transit (top) and during the occultation
(bottom). The impact parameters b and the transit parameters (δ, t_F, t_T) used in the
equations here after are indicated on this figure.

Seager & Mallén-Ornelas (2003) give a set of simple analytical equations to derive
the following planet parameters: $R_{\rm p}/R_\star$ the planet radius relative to the radius of the
host star, $a/R_\star$ the orbital distance of the planet relative to the radius of the host star, i
the orbital inclination projected to the plane of the sky. Under the approximations listed
herafter, these planet parameters can be derived from the following four observables
of the transit light curve: P the orbital period, δ the transit depth, t_F the duration of the

transit when the planet disk is completely inside the stellar disk, and t_T the total transit duration.

1. The planet is in a circular orbit. This is often true for planets close to their star as tidal interaction with the star acts to circularise the orbit of the planet.

2. The stellar intensity is uniform across the stellar disk, i.e. the stellar limb darkening is negligible. This is true at long wavelengths, e.g. the I band (806±149 nm).

3. The planet is dark compared to the central star.

4. The light comes from a single star, i.e the light from the planet host star is not blended with the light from another star.

To gain a useful insight into the transit geometry, it is interesting to reproduce here the analytic equations given by Seager & Mallén-Ornelas (2003) for the planet-to-star radius ratio $R_p/R_\star$ (equation 1.2), the planet impact parameter b (equation 1.7), the planet orbital distance relative to the stellar radius $a/R_\star$ (equation 1.9), and the planet orbital inclination projected onto the plane of the sky i (equation 1.12). The planet orbital period is measured from the time difference between successive transits, which requires a light curve with at least two transits. But under the above conditions, Seager & Mallén-Ornelas (2003) show that if the stellar mass and radius are know (e.g. from spectral type analysis), the transit period can be estimated from a single-transit light curve (equation 1.15). Under the approximation that $M_p \ll M_\star$, the stellar density $M_\star/R_\star^3$ can also be derived from the transit light curve (equation 1.13). Under the assumption that $a \gg R_\star$, some of the equations can be simplified (see equations 1.8, 1.10, 1.14, 1.16).

The transit depth δ normalised by the stellar luminosity $L_\star$, assuming no stellar limb darkening, a dark planet, and no stellar blend, is

$$\delta = \frac{L_\star - L_{\star,\ with\ planet\ in\ transit}}{L_\star} \tag{1.1}$$

As $L_\star = \pi R_\star^2 F_\star$ and $L_{\star,\ with\ planet\ in\ transit} = L_\star - \pi R_p^2 F_\star)$, where $R_\star$ and $F_\star$ are the stellar radius and stellar flux per unit surface area, and R_p is the planet radius, the transit depth is related to the planet-to-star radius ratio as follows

$$\delta = \left(\frac{R_p}{R_\star}\right)^2 \tag{1.2}$$

The transit shape – equivalent to the transit duration inside the ingress and egress relative to the total transit duration – can be derived as follows

$$\left(\frac{\sin\left(t_F \pi/P\right)}{\sin\left(t_T \pi/P\right)}\right)^2 = \frac{[1 - R_p/R_\star]^2 - [a/R_\star\ \cos i]^2}{[1 + R_p/R_\star]^2 - [a/R_\star\ \cos i]^2} \tag{1.3}$$

Under the approximation that $a >> R_\star$, $t_T\pi/P << 1$, and as for small x, $\sin x \simeq x$, the equation 1.3 simplifies to

$$\left(\frac{t_F}{t_T}\right)^2 = \frac{[1 - R_p/R_\star]^2 - [a/R_\star \; \cos i]^2}{[1 + R_p/R_\star]^2 - [a/R_\star \; \cos i]^2} \tag{1.4}$$

The total transit duration t_T can be derived as follows

$$t_T = \frac{P}{\pi} \sin^{-1} \left(\frac{R_\star}{a} \frac{\sqrt{[1 + R_p/R_\star]^2 - [a/R_\star \; \cos i]^2}}{\sin i} \right) \tag{1.5}$$

Under the approximation that $a >> R_\star$, $\cos i << 1$, and as for small x, $\arcsin x \simeq x$, and the equation 1.5 simplifies to

$$t_T = \frac{P \; R_\star}{\pi \; a} \sqrt{\left(1 + \frac{R_p}{R_\star}\right)^2 - \left(\frac{a}{R_\star} \; \cos i\right)^2} \tag{1.6}$$

From equations 1.5 and 1.2, the impact parameter b – projected distance between the planet and star centres – can be derived from the light curve parameters as follows

$$b \equiv \frac{a}{R_\star} \cos i = \sqrt{\frac{(1 - \sqrt{\delta})^2 - [\sin^2(t_F\pi/P)/\sin^2(t_T\pi/P)](1 + \sqrt{\delta})^2}{1 - [\sin^2(t_F\pi/P)/\sin^2(t_T\pi/P)]}} \tag{1.7}$$

Under the approximation that $a >> R_\star$, $t_T\pi/P << 1$, and the equation 1.7 simplifies to

$$b = \sqrt{\frac{(1 - \sqrt{\delta})^2 - (t_F/t_T)^2](1 + \sqrt{\delta})^2}{1 - (t_F/t_T)^2}} \tag{1.8}$$

The planet orbital distance normalised by the stellar radius $a/R_\star$

$$\frac{a}{R_\star} = \sqrt{\frac{(1 + \sqrt{\delta})^2 - b^2[1 - \sin^2(t_T\pi/P)]}{\sin^2(t_T\pi/P)}} \tag{1.9}$$

Under the approximation that $a >> R_\star$, from equation 1.6 and 1.8, $a/R_\star$ can be expressed more simply as follows

$$\frac{a}{R_\star} = \frac{2P}{\pi} \frac{\delta^{1/4}}{\sqrt{t_T^2 - t_F^2}} \tag{1.10}$$

Using Kepler's 3rd law[7] ($\frac{P^2}{4\pi^2} = \frac{a^3}{G(M_\star + M_p)}$), where G is the gravitational constant, and under the approximation that $M_p << M_\star$, the planet orbital distance a can also be derived as

$$a = \left(\frac{P^2 G M_\star}{4\pi^2} \right)^{1/3}$$ (1.11)

From the definition of b (equation 1.7), the planet orbital inclination projected onto the plane of the sky, i, can be derived as

$$i = \cos^{-1} \left(b \frac{R_\star}{a} \right)$$ (1.12)

Using Kepler's 3rd law under the approximation that $M_p << M_\star$, and equation 1.9, the stellar density $\rho_\star$ defined as follows, can be derived from the light curve parameters.

$$\rho_\star \equiv \frac{M_\star}{R_\star^3} = \frac{4\pi^2}{P^2 G} \left(\frac{a}{R_\star} \right)^3 = \frac{4\pi^2}{P^2 G} \left(\frac{(1 + \sqrt{\delta})^2 - b^2[1 - \sin^2(t_T \pi / P)]}{\sin^2(t_T \pi / P)} \right)^{3/2}$$ (1.13)

Under the approximation that $a >> R_\star$ and that $M_p << M_\star$, using Kepler's 3rd law and equation 1.10, $\rho_\star$ can be expressed more simply as follows

$$\rho_\star = \frac{32 P}{G\pi} \frac{\delta^{3/4}}{(t_T^2 - t_F^2)^{3/2}}$$ (1.14)

Under the approximation that $M_p << M_\star$, reversing equation 1.13, if the stellar mass and radius are known, the planet orbital period can be derived from a single-transit light curve as follows

$$P = \sqrt{\frac{R_\star^3}{M_\star} \frac{4\pi^2}{G} \left(\frac{(1 + \sqrt{\delta})^2 - b^2[1 - \sin^2(t_T \pi / P)]}{\sin^2(t_T \pi / P)} \right)^{3/2}}$$ (1.15)

The equation of P simplifies to the following one, under the approximation that $a >> R_\star$, using Kepler's 3rd law under the approximation that $M_p << M_\star$ and equation 1.14.

$$P = \frac{M_\star}{R_\star^3} \frac{G\pi}{32} \frac{(t_T^2 - t_F^2)^{3/2}}{\delta^{3/4}}$$ (1.16)

Equations for an eccentric orbit

The equations presented above can be used to derive the planet parameters from the transit light curve of a planet in a circular orbit. The equation to derive the planet-

---

[7]Kepler's 3rd law: "The square of the orbital period of a planet is directly proportional to the cube of the semi-major axis of its orbit."

to-star radius ratio $R_\mathrm{p}/R_\star$ is the same for a circular and for an eccentric orbit, as the equation is not dependent on the eccentricity e and the argument of periastron ω. The elements of an eccentric orbit used here after are as defined in Figure 1.3.
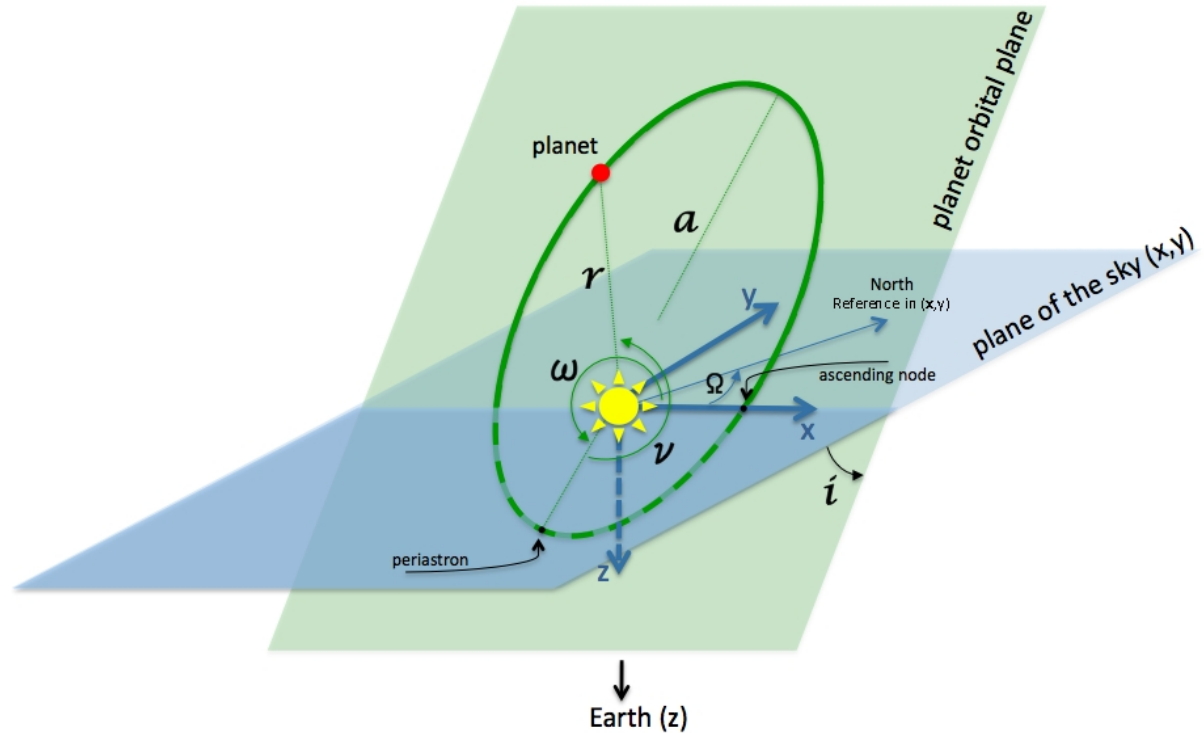

Figure 1.3: Sketch of a planet in an eccentric orbit around its host star. a is the semi-major axis of the planet's orbit, r is the planet to star distance, i is the inclination of the planet's orbit with regards to the plane of the sky, ν is the true anomaly of the planet (i.e. the position angle from the periastron of the planet in its orbit), ω is the argument of periastron of the planet's orbit (i.e. the position angle of the periastron from the ascending node where the planet moves North through the plane of the sky) and Ω is the longitude of the ascending node (i.e. the angle in the plane of the sky between the North direction and the ascending node). The North is a reference direction in the plane of the sky corresponding to the direction of the North pole projected onto this plane.

Kepler's 1st law[8] defines the equation of an ellipse. Applied to exoplanets, this gives the following relation for the star-planet distance r in an eccentric orbit:

$$r = \frac{a(1 - e^2)}{1 + e\cos\nu} \tag{1.17}$$

where a is the semi-major axis of the orbit, e is the eccentricity of the orbit ($e = \sqrt{1 - \left(\frac{b}{a}\right)^2}$ with b the semi-minor axis of the orbit), and ν is the true anomaly (the angle between the direction to the ascending node and the direction to the position of the planet in the orbit, see Figure 1.3).

---

[8]Kepler's 1st law: "The orbit of every planet is an ellipse with the Sun at a focus"

If the planet transits its host star, the orbital inclination $i \approx 90^o$, and the true anomaly of the planet at mid-transit can be simplified to $\nu_c = \pm\frac{\pi}{2} - \omega$ ("+" for mid-transit and "-" for mid-occultation). As $\cos\left(\pm\frac{\pi}{2} - \omega\right) = \pm\sin\omega$, the star-planet distance at conjunction r_c can be expressed as

$$r_c = \frac{a(1 - e^2)}{1 \pm e\sin\omega} \tag{1.18}$$

The impact parameter is $b \equiv \frac{r_c}{R_\star}\cos i$ (same definition as in equation 1.7 but replacing a by r_c). Using equation 1.18, b can thus be expressed for an eccentric orbit as follows

$$b = \frac{a}{R_\star}\cos i \left(\frac{1 - e^2}{1 \pm e\sin\omega}\right) \tag{1.19}$$

This equation compares to the definition of b in a circular orbit (equation 1.7) by multiplying this expression by $\frac{1-e^2}{1\pm e\sin\omega}$ ("+" for mid-transit and "-" for mid-occultation).

t_T and t_F for an eccentric orbit should be solved numerically using Kepler's equations (Equation 1.27). Winn (2010) proposes, as a good approximation for eccentric orbits, to multiple t_T and t_F (calculated with the eccentric expression of b) by the following factor which accounts for the altered sky-projected speed of the planet at conjunction:

$$\frac{\dot{X}(\nu_c)\,[e=0]}{\dot{X}(\nu_c)} = \frac{\sqrt{1 - e^2})}{1 \pm e\sin\omega} \tag{1.20}$$

where X is the position of the planet in the plane of the sky along the axis towards the ascending node (see Figure 1.3), $\dot{X}(\nu_c)$ is the velocity of the planet along this axis at conjunction ("+" is for mid-transit and the "-" for mid-occultation), and $\dot{X}(\nu_c)\,[e=0]$ is the value of this velocity for a circular orbit.

Limb darkening

In reality, the stellar luminosity is not constant across the stellar disk. The stellar disk is brighter at its centre than at its edge. The photons received from the centre of the stellar disk come from deeper into the stellar atmosphere than those received from the edge of the disk. A photon coming from deeper into the stellar atmosphere has a higher temperature and thus appears brighter at the associated wavelength. Thus, at the corresponding wavelength, the stellar centre appears brighter than the stellar limb, hence the expression "limb darkening".

Using a realistic model of stellar limb darkening is important when fitting transit light curves, as the shape of the limb darkening will influence the derived planet parameters (mainly the planet radius and impact parameter on the stellar disk).

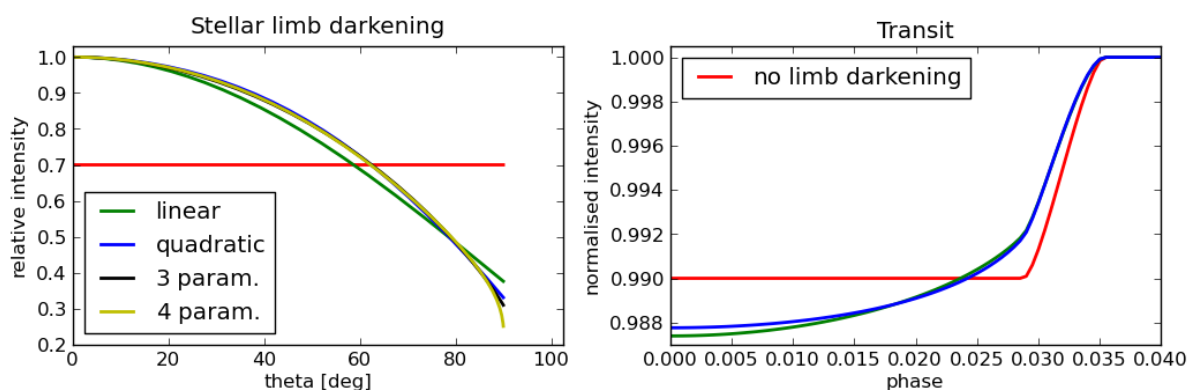There are different limb darkening laws proposed in the literature to model the varia-

Figure 1.4: Left panel: Solar limb darkening in CoRoT bandpass with the linear law (green), the quadratic law (blue), the non-linear 3 parameter law (black), and the non-linear 4 parameter law (yellow). Right panel: The second half of the phase-folded transit of a Jupiter-size planet at $a/R_\star$=5 of a solar type star (T_{eff}=5800K, $\log g$=4.5, (M/H)=0.0) seen in the CoRoT bandpass with no stellar limb darkening (red), a quadratic stellar limb darkening (blue) and a linear stellar limb darkening (green).

tion of intensity across the stellar disk: e.g. the linear law, the quadratic law, the square root law, the logarithmic law, the non-linear law (Claret 2000), and the 3-parameters non-linear law (Sing 2010). To date, the most commonly used when fitting transiting exoplanet light curves are the linear, the quadratic and the non-linear laws. In light curves with high precision photometry, the linear law is insufficient to correctly reproduce the intensity variation over the stellar disk (e.g. Brown et al. 2001). The quadratic law is valid in certain ranges of stellar effective temperatures; for main sequence stars this law is accurate within 3% of the transit depth (Mandel & Agol, 2002) which can become insufficient to model high precision photometry light curves (e.g. bright stars observed with HST, CoRoT or Kepler). The non-linear law is valid over a large range of stellar models. The 3-parameter non-linear law was introduced to better reproduce the limb darkening at small angles θ (angle between the line of sight and the emergent intensity). This law is very similar to the non-linear law but does not model a sharp drop in luminosity at small μ.

This intensity variation across the stellar disk is calculated from stellar atmosphere models (e.g. ATLAS9[9], PHOENIX[10]) where the emergent intensity with regard to the line of sight is known. This intensity is then passed through different instrumental filters (e.g. the standard filters in Claret 2000 and Claret 2004, and the CoRoT and Kepler filters in Sing 2010), and fitted with different limb darkening laws to derive the associated limb darkening coefficients.

---

[9]http://kurucz.harvard.edu/grids.html
[10]http://www.hs.uni-hamburg.de/EN/For/ThA/phoenix/index.html

The linear law:

$$\frac{I(\mu)}{I(\mu = 1)} = 1 - u(1 - \mu) \tag{1.21}$$

The quadratic law:

$$\frac{I(\mu)}{I(\mu = 1)} = 1 - u_a(1 - \mu) - u_b(1 - \mu)^2 \tag{1.22}$$

The non-linear law:

$$\frac{I(\mu)}{I(\mu = 1)} = 1 - u_1(1 - \mu^{1/2}) - u_2(1 - \mu) - u_3(1 - \mu^{3/2}) - u_4(1 - \mu^2) \tag{1.23}$$

The 3-parameter non-linear law:

$$\frac{I(\mu)}{I(\mu = 1)} = 1 - u_2(1 - \mu) - u_3(1 - \mu^{3/2}) - u_4(1 - \mu^2) \tag{1.24}$$

where, $I(\mu = 1)$ is the intensity at the centre of the stellar disk, $\mu = cos(\theta)$ with θ the angle between the line of sight and the emergent star light, u is the linear limb darkening coefficients, u_a and u_b are the quadratic limb darkening coefficients, and u_n are the limb darkening coefficients of the non-linear law.

In practice, the choice of which limb-darkening law to use depends on the signal-to-noise ratio (S/N) of the transit, the observational bandpass and the stellar type. High S/N observations allow the shape of the limb darkening to be more accurately constrained, and so can justify the usage of a limb-darkening law with more coefficients.

Equations for a non-uniform intensity across the stellar disk

Mandel & Agol (2002) give a list of analytic functions to model transit light curves which include limb-darkening (quadratic and non-linear laws). The function to be used depends on the size (radius) of the planet relative to the star and on the position of the planet on the stellar disk. The exact analytic formulae are given in Mandel & Agol (2002), as well as a simpler version (less computing time) valid for small planets ($\frac{R_\mathrm{P}}{R_\star} \leq 0.1$) where the stellar brightness under the disk of the planet can be approximated as a constant.

Giménez (2006) also presents analytic functions to model the transit light curves. There is little difference between their formalism and that of Mandel & Agol (2002).

Throughout this thesis, I perform the modelling of transit light curves using the analytical equations of Mandel & Agol (2002) for transit light curves with quadratic limb darkening (or linear limb darkening by setting the second coefficient of the quadratic law to zero). Eric Agol kindly provides an IDL implementation of their formulae[11], which I made use of in Chapters 2 and 3.

---

[11] http://www.astro.washington.edu/users/agol

1.3.2   Analytic equations for the radial velocity variations of a star due to an orbiting planet

The equations listed in this subsection are based on those given in the Celestial Mechanics chapter of J. B. Tatum[12].

The equation for radial velocity variations V of a star due to an orbiting planet is derived as:

$$V = V_0 + K_\star(\cos{(\omega_\star + \nu_\star)} + e\cos{\omega_\star}) \tag{1.25}$$

where V_0 is the mean radial velocity of the star-planet centre of mass with regards to the observer, $K_\star$ is the semi-amplitude of the radial velocity variations, $\omega_\star$ is the argument of periastron of the star's orbit around the star-planet centre of mass ($\omega_\star = \omega_p + \pi$), $\nu_\star$ is the true anomaly of the position of the star on its orbit around the star-planet centre of mass ($\nu_\star = \nu_p + \pi$), and e is the eccentricity of the stellar orbit (same as that of the eccentricity of the planet's orbit).

Equation 1.25 is a function of the true anomaly which is itself a function of time. To solve this equation, the true anomaly needs to be known. This is done by using the mean anomaly M (equation 1.26) to derive the eccentric anomaly E (equation 1.27), which is then used to derive the true anomaly ν (equations 1.29 and 1.30).

The mean anomaly M at a time t (angle covered at the average angular speed $\frac{2\pi}{P}$ since the last passage at periastron) is defined as:

$$M = \frac{2\pi}{P}(t - T) \tag{1.26}$$

where P is the orbital period of the planet and T is the time at the last passage at the periastron.

The eccentric anomaly E (projection of the true anomaly on a circle with radius equal to the orbital semi-major axis) can be derived from Kepler's equation:

$$M = E - e\sin{E} \tag{1.27}$$

where, e is the eccentricity of the orbit.

This equation cannot be solved analytically and is solved numerically, e.g. using the Newton-Raphson method. This method consists of finding a better value at each iteration using the value found at the previous iteration, the expression of the function and its derivative: $x_{n+1} = x_n - \frac{f(x_n)}{f'(x_n)}$. In the present case of deriving the eccentric anomaly

---

[12]http://astrowww.phys.uvic.ca/~tatum/celmechs.html

E, $f(E_n) = E_n - e \sin E_n - M$ which becomes:

$$E_{n+1} = \frac{M - e(E_n \cos E_n - \sin E_n)}{1 - e \cos E_n} \qquad (1.28)$$

The true anomaly is related to the eccentric anomaly through the following equations:

$$\cos \nu = \frac{\cos E - e}{1 - e \cos E} \qquad (1.29)$$

$$\sin \nu = \frac{\sqrt{1 - e^2} \sin E}{1 - e \cos E} \qquad (1.30)$$

The mass of the planet M_p relative to the mass of its host star $M_\star$ can be derived as follows, using the $K_\star$ measured from the radial velocity curve of the star (see Figure 1.5):

$$\frac{M_p \sin i}{(M_\star + M_p)^{2/3}} = K_\star \left(\frac{P}{2\pi G} \right)^{1/3} \sqrt{1 - e^2} \qquad (1.31)$$

where i is the orbital inclination and G is the gravitational constant. If $M_p << M_\star$ then:

$$M_p \sin i = K_\star \left(\frac{P M_\star^2}{2\pi G} \right)^{1/3} \sqrt{1 - e^2} \qquad (1.32)$$

When a planet transits in front of its star, it creates during the transit a perturbation in the radial velocity (RV) variations of the host star (see Figure 1.5). This effect is called the Rossiter-McLaughlin (RM) effect. The shape of the perturbation depends on the inclination of the planet's orbital plane to the stellar spin axis. For transiting planets small in mass and/or with large orbits, the planet can create a larger amplitude RM effect than the RV variations of its star. Combined with the fact that the RM variation occurs on a shorter timescale than the RV variation, the RM effect will be a useful tool to confirm the planetary nature of small transiting planets orbiting in large orbits (Gaudi & Winn, 2007).
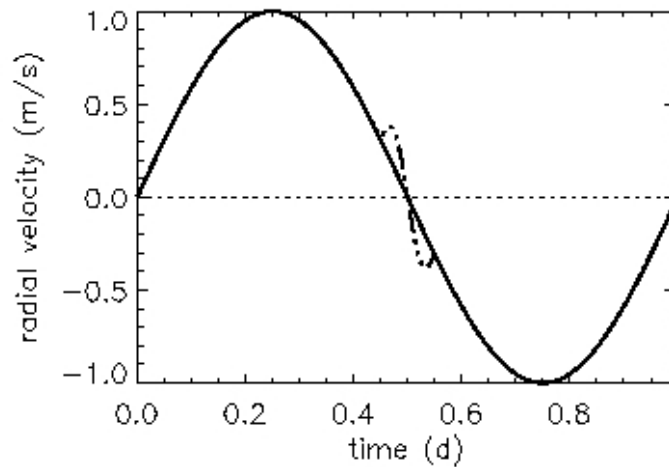
Figure 1.5: The radial velocity curve of a star orbited by a planet a few times more massive than the Earth, in a circular orbit (black line). The semi-amplitude of the radial velocity variation is called K, the period of the variation is the planet orbital period P. Here, $P = 1$, $K = 1$, and the mid-transit is at 0.5 d. The dashed-dotted blip is the spectroscopic transit of the planet, called the Rossiter-McLaughlin effect, which adds up to the star's radial velocity curve if the planet transits the stellar disk. Here, the sky-projected spin axis of the planet's orbit projected onto the sky is aligned with the sky-projected stellar rotation axis.

1.3.3 Planetary atmospheres

Transmission spectroscopy of a planet's atmosphere can be performed during its transit. Emission spectroscopy of a planet's disk can be performed during occultation, where light from the star and the planet can be separated. In addition the planet's orbital phase variations can be observed. The above techniques allow the study of some properties of the planet, such as the chemical composition of the planet's atmosphere, the planet's atmospheric circulation, the presence of clouds or hazes, the thermal emission of the planet, and the planet's albedo.

The transmitted spectrum of the upper atmosphere of an exoplanet is obtained by observing the transit of the planet in different wavelengths. Some chemical elements in the atmosphere will strongly absorb particular wavelengths of the starlight that pass through the planet's atmosphere, this makes the planet appear larger at these wavelengths. This type of observations has been performed from space using the Hubble Space Telescope (HST).

When planets are occulted by their star, the loss in received brightness is due to the planet's emission being obstructed by the star. The planet's emission has a component of stellar reflected light and a component of thermal emission. The thermal emission of the planet can be studied by measuring the depth of the occultation at long wavelengths (e.g. in the I band and at redder wavelengths) where it dominates

over the stellar reflected light component. The first approximation made to derive the temperature of the planet, is to consider that the planet emits like a black body. In reality, if some of the planet's thermal flux is absorbed by molecules in its atmosphere, at this wavelength the depth of the occultation will appear smaller, thus giving a smaller temperature. Observing the occultation at multiple long wavelengths would allow the observation of the shape of the planet's black body due to thermal emission, and to derive a more realistic planet temperature. For instance, observations of the occultation of some transiting exoplanets have been made from space with the Spitzer Space Telescope (SST), and from the ground with the Very Large Telescopes (VLT) and soon the Gran Telescopio Canarias (GTC).

When observing the occultation of an exoplanet at shorter wavelength (e.g. in the optical), the dominant component of the planet emission is the stellar reflected light. The depth of the occultation due to the loss of the stellar light reflected by the planet, allows one to derive the albedo of the planet. However, if the planet's thermal emission is not negligible at the observed wavelength, the albedo cannot be uniquely calculated from the depth of the planet's occultation at only one wavelength. If multiple short and mid wavelength observations of the depth of the planet's occultation can be performed, then the wavelenght distribution of reflected stellar light and of the planet thermal emission can be obtained. These two components of the planet's flux can then be separated from each other, and both the albedo and the thermal emission can be extracted. For instance, observations of exoplanet occultations in the optical have been performed from space using CoRoT and Kepler, and from the ground using the VLT for instance.

Differential spectroscopy consists of taking the spectrum of the light received from the star-only during the planet's occultation, and from the star-and-planet when the planet emerges from the occultation. By comparing the two spectra, one can extract a low-signal emission spectrum of the planet.

When the photometric orbit of the exoplanet is followed from one transit to the next, the orbital phases of the planet – variation in flux due to the varying visible fraction of the planet's day-side – can be observed. At long wavelengths, if the phase of the maximum of this modulation is shifted from the phase of the planet's occultation, it indicates that strong winds in the planet's atmosphere are blowing the point of maximum heat on the planet away from the point directly facing the host star. This is a measurement of the planet's atmospheric circulation. At short wavelengths, the phase modulation of the planet depends on the properties of the particle reflecting the light. Ice has a uniform phase function as it has the same intensity seen from different angles, whilst water has a more complicated phase function, as for instance oceans appear darker seen from directly above than from an angle.

The amplitude of all the effects mentioned above can be two orders of magnitude smaller than the planet's transit signal (depending on the eccentricity of the orbit, the

size of the planet and its distance to the host star), and their observation requires high precision photometry (large collecting area, stable instruments).

1.4 Challenges for the detection and characterisation of exo-planets

Limitations in the detection and characterisation of an exoplanet can come from different sources, and depend on each planet, star and instrument used. For instance, the characterisation of CoRoT-7b is limited by stellar activity affecting the measure of the mass of the planet, whilst the characterisation of the OGLE planets is limited by the poor determination of the stellar parameters due to the star's faintness.

1.4.1 Stellar systems mimicking planetary transits

Stellar systems mimicking planetary transits create false alarms in the search for transiting exoplanets. The systems of stars that can create planetary-transit-like light curves are listed bellow.

Small stars, brown dwarfs and gas giant planets have similar sizes, so have similar transit depths in a light curve. However, as these objects have different masses, they can be differentiated using radial velocity measurements of their host stars to derive the mass of the transiting object. OGLE-TR-122 is an example of a planetary-like candidate discovered using the transit method and confirmed by radial velocity measurements to be a low mass star (Pont et al., 2005).

If the host star is a giant star, a Jupiter-like transit depth (1%) would be caused by a stellar companion and not a planet. This is due to the fact that the transit depth gives the radius of the companion relative to the radius its host star, so for the same transit depth, a larger star means a larger companion. This false detection can be ruled out from the transit light curve which allows one to derive an estimate of the stellar density $M_\star^{1/3}/R_\star$ (Seager & Mallén-Ornelas, 2003), giant stars being less dense than main sequence stars as they have a larger radius.

Grazing binaries are another source of false detections as only a fraction of the disk of the transiting star crosses the stellar disk, causing the transit to be shallower and thus more planetary-like. These events can be identified from the light curve by analysing the shape of the transit, as grazing binaries have V-shaped transits and planetary transits are more U-shaped (due to limb darkening and radius ratio).

An eclipsing binary pair blended with a third star physically associated (triple system) or aligned by chance in the line of sight (background or foreground eclipsing binaries), can mimic a planet transit light curve as the real depth of the eclipse is diluted by the light of the third star. A case of an eclipsing binary pair blended with a third

star can be identified by detecting a double peak when cross-correlating the spectra of the blended stars with model stellar spectra, or by resolving the blend with high spatial resolution imaging (e.g. WASP-9b was retracted from the list of planets as later, through spectroscopy, identified as the member of a stellar binary). For high precision photometry light curves, another method is to compare the stellar density derived from the light curve (equation 1.13) with the stellar density derived from the observed spectral type; if the two are very different it indicates that the transit is diluted by the light of another star (Seager & Mallén-Ornelas, 2003).

Colour photometry can also be used to differentiate between a planetary transit and an eclipsing binary (e.g Tingley 2004) as the transit depth of planets will be quasi colour independent (the planet is dark compared to its host star), while the transit of a star is colour dependent and will have different depths at different wavelengths.

1.4.2 Systematics

The noise in a light curve is not purely gaussian (white noise), but has a component of correlated noise (red noise, Pont et al. 2006) mainly due to atmospheric effects for ground observations (e.g. scintillation, transparency variations, over-flights of satellites and planes, moon), or to instrumental effects for space observations (e.g. hot pixels due to cosmic rays, telescope jitters due to thermal shocks or battery ignitions).

Systematics in the transit light curve reduce the detectability of planets and limit the characterisation of the planet. These systematics can be instrumental, and/or atmospheric when observing from the ground. For instance, in the detailed analysis of the CoRoT light curves in Chapter 4, hot pixels create systematic noise which are difficult to filter out in an automated way and which affect the detection of low amplitude signals such as secondary eclipses and planet orbital phases.

1.4.3 Stellar activity

Stellar variability is another source of correlated noise superimposed onto the planet signal in the stellar light curve and radial velocity curve.

Stellar variability is caused by physical processes which have different time scales. Stellar magnetic activity, i.e. variations in magnetic field lines over time, is the main cause of stellar variation. The magnetic field is created by the dynamo effect of moving charged particles in the stellar plasma, e.g. due to differential rotation between the stellar core and the stellar convective envelope for main sequence stars. The differential rotation also causes magnetic lines to twist and break allowing the material trapped in the field of the broken magnetic line to rise and emerge from the stellar surface carrying hot material out, and cooled material back into the stellar surface. The regions where the hot material emerges from the sub-surface, along the field lines, appear brighter (plages). The regions where the cooled material sinks back into the

stellar surface, along the field lines, appear darker (spots). As the star rotates, the stellar spots and plages appear and disappear on the visible side of the star, which changes the stellar brightness at the timescale of the stellar rotation. The number of spots and plages also evolve in time over longer timescales (e.g. the 11-years solar activity cycle). These magnetic-field-induced stellar variations produce photometric and spectroscopic stellar variability on time scales from days to weeks (stellar rotation) and from month to years (stellar activity cycles). The amplitudes of these variations are larger than the that of the two other processes described hereafter, and is comparable or larger than the amplitude of planetary transits.

Stellar granulations arise from the convection of hot material being brought from the stellar subsurface to the surface, due to thermal difference between the two surfaces. This process creates variations in stellar brightness at shorter time scales (hours).

Stellar oscillations are due to the displacement of stellar material under the convection which produces pressure and gravity waves on the material of the stellar surface. This process creates stellar variability at higher frequencies (minutes).

Stellar activity is dependent on stellar type/mass, and stellar age. This dependence comes from the internal structure of the star along with the presence, size, and position of a stellar convective envelope. Stars with smaller convection envelopes (e.g. massive stars emitting more flux), will show smaller level of activity.

The dependence on stellar age comes from the stellar rotation rate driving the differential rotation between the stellar core and the convective envelope, which is the magnetic field production mechanism for main sequence stars (stars with a hydrogen burning core). Stars rotating faster display a higher activity level. Young stars have larger rotation rates (i.e. are more active) as they have gained angular momentum through contraction under the gravity.

The dependence on mass also comes from the ability for the star to form a radiative core, as radiative pressure will halt the stellar contraction. The stars then stop gaining angular momentum, and the dissipation of its angular momentum (e.g. though disk locking) will force the star to spin down, thus reducing the activity level for older stars. Lower mass stars ($M_\star < 0.5 M_\odot$) will not start the hydrogen burning phase, will not develop a radiative core, and will maintain their activity level longer. As a comparison, the Sun (G-type on the main sequence) is a relatively aged star, it is a slow rotator and has a low level of activity.

Favata & Micela (2003), Schrijver & Zwaan (2000) and Aigrain et al. (2004) provide detailed information on the dependency of stellar activity with stellar type, mass and age, and on the physical processes behind the different timescales of the stellar activity.

The photometric and radial velocity amplitude of stellar variability can easily be larger than the amplitude of the signal of a planet, which can affect the detection of the later by creating false alarms and reducing the amplitude of the real signal, especially in the regime of small planets (see Jenkins 2002 for a study on the impact of

solar-like variability on the detectability of transiting exoplanets). Stellar variability also hinders the characterisation of the detected planets as it adds correlated noise to the planet signal, reducing the precision and altering the accuracy of the derived planet parameters.

As the star rotates, a stellar spot on its surface will hide a part of the stellar surface rotating towards us and then a part rotating away from us, creating red-shifted and blue-shifted perturbations respectively. To identify radial velocity variations due to stellar activity and remove it to some extent, several techniques are combined (see Boisse et al. 2009 for a detail explanation and application of these techniques). To average over the high frequencies of the stellar activity due to oscillations for instance, longer exposures ($\sim$1h) can be taken. To remove the stellar activity components due to granulation, a boxcar smoothening (few hours) can be applied. The stellar activity component due to spots and plages are more difficult to remove as their amplitude in radial velocity can be larger than that of the planet signal. Techniques to identify radial velocity variations due to stellar activity at long times scales include the photometric follow-up of the star simultaneous to the radial velocity measurements, the analysis of the correlation between the radial velocity variations and the variations in the bisector of the cross-correlation peak of the stellar spectra, or with the variations in CaII H&K lines, H$_\alpha$ line and HeI line (spectroscopic indices for stellar activity).

Different filters are used by different teams to remove the photometric stellar variability from the stellar light curves due to the flux variations intrinsic to the star. Unfortunately, these filters degrade the information on the transit shape, as the transit signal and the stellar activity frequency domains overlap. This results in the physical parameters of the planet being mis-estimated. This is discussed in the Chapter 2 and a new method to filter the stellar variability with minimum alteration to the transit signal is then presented.

The stellar variability can also affect the observation of the atmosphere of the exoplanet. The variation in stellar flux due to the activity is chromatic, so the multi-wavelength observations of the planet's transit and occultation need to be performed over an interval of time shorter than the timescale of the stellar variability.

1.4.4   Uncertainties on the planet parameters

The uncertainties in the mass, radius, and inclination of a planet depend on the uncertainties of the host star's mass and radius ($M_\star$, $R_\star$), on the uncertainties on the transit parameters (δ, t_F, t_T), and on the uncertainties on the radial velocity measurements. For large planets (larger than Jupiter), the uncertainties on the planet mass and radius are mainly due to the uncertainties on the stellar parameters. For smaller planets (smaller than Uranus) around active stars, the uncertainties on the planet mass and radius can be dominated by the uncertainties on the transit parameters. Figure 1.6 shows the contribution to the uncertainties in a planet's mass and radius coming from

the stellar parameters (in blue) and from the transit parameters (in black).
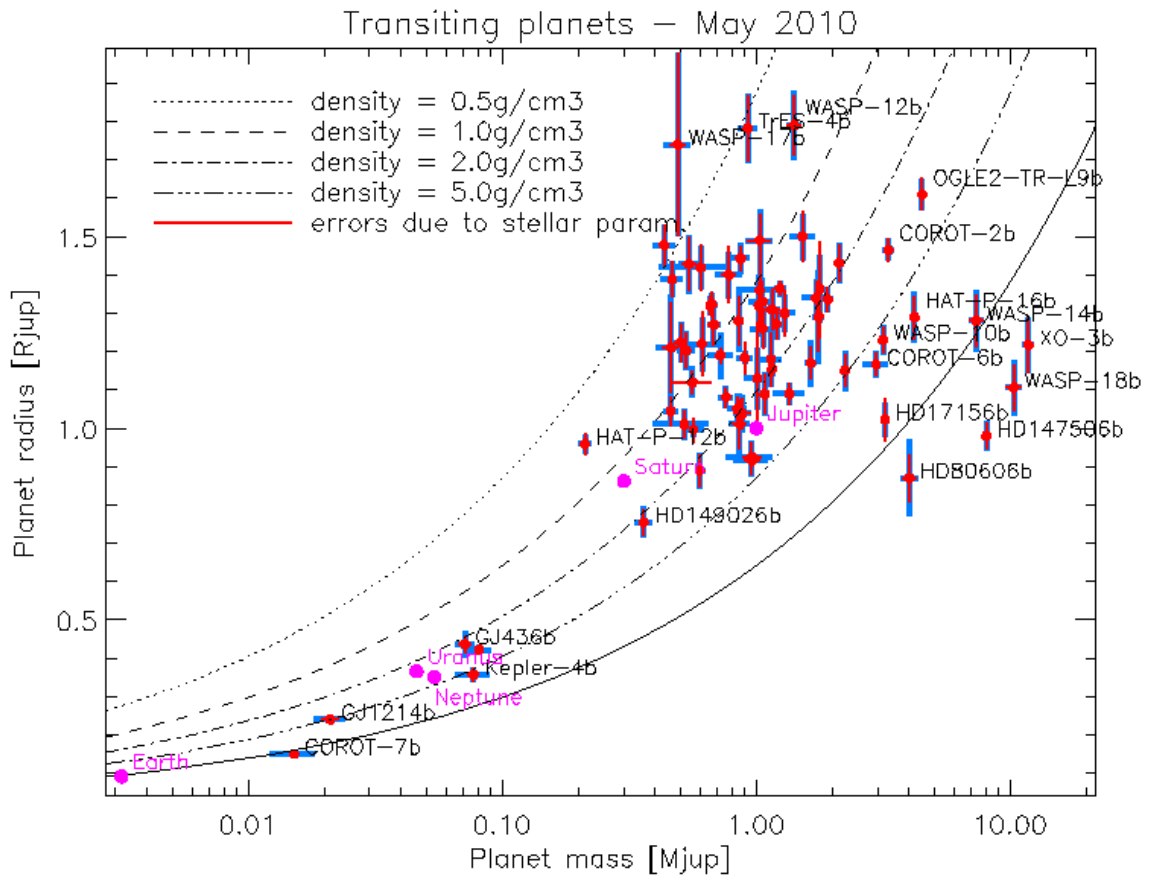

Figure 1.6: Mass-radius diagram of the transiting planets discovered to date (May 21th 2010) with the error bars on the planet's mass and radius with the contribution from the uncertainties in the transit parameters (black) and the contribution from the uncertainties in the stellar parameters (blue). The planet masses and radii are taken from http://www.inscience.ch/transits/, except for CoRoT-7b which is taken from http://exoplanet.eu/catalog-transit.php. The uncertainties in the planet parameters due to the stellar parameters are calculated by propagating the uncertainties in the stellar parameters assuming the measurements for the transit and radial velocity curves have no uncertainty.

1.5 Instruments for the detection and characterisation of transiting exoplanets

1.5.1 Current

CoRoT (COnvection ROtation and planetary Transits), is a French-ESA (European Space Agency) satellite with 27-cm diameter mirror and a 3x3^o field of view. It has been in orbit around the Earth since December 2006 and searches for short period exoplanets with radii down to few times that of the Earth. CoRoT looks at stars with V magnitude in the range 11 to 16 V, in 4 different areas in the galactic plane each year (20 to 150 days on each field). In this thesis, the light curves of the CoRoT planets are studied.

Kepler is a NASA (National Aeronautics and Space Administration) satellite with a 95-cm diameter mirror and a 10° field of view. It has been in an Earth-trailing heliocentric orbit since March 2009 and searches for exoplanets similar to the Earth in terms of size, orbital distance and stellar host type. Kepler looks at stars with V magnitude in the range of 9 to 16, in a single area of the sky (continuously for 3.5 years).

In 2009, CoRoT found a close-in Earth-like planet around a solar type star, and Kepler is expected to detect several more of these. Follow-up observations of these objects, for mass measurement and atmosphere characterisation, are challenging as these planets are small compared to their host stars. For smaller stars, e.g. M-dwarfs ($\sim0.1 M_\odot$, $\sim0.1 R_\odot$, ~3000 K), an Earth-size planet in the habitable zone[13] will have a larger radius ratio and mass ratio with its star and will be closer to the star, making its transit and gravitational tug easier to detect. The atmosphere of these Earth-size planets will also be easier to detect through transmission spectroscopy as the atmosphere can be thicker for lower mass, lower gravity planets. MEarth is a ground-based mission with a set of eight 40-cm telescopes searching for super-Earths around small stars. RoPACS (Rocky Planets Around Cool Stars) is a network using the UKIRT (United Kingdom Infrared Telescope) to search for transiting planets around cool stars.

SuperWASP (Wide Angle Search for Planets) and HATNet (Hungarian Automated Telescope Network) are ground based missions searching for transiting exoplanets around bright stars across the sky (~9 mag).

Precise radial velocity measurements are currently done with the HARPS spectrograph on the 3.6 m telescope at ESO-La Silla Observatory in Chile, and with the HIRES (High Resolution Echelle Spectrometer) spectrograph on the 10 m Keck-1 telescope at the Keck Observatory in Hawaii. With these current high-resolution spectrographs, stellar radial velocity variations down to 0.3 to 1 ms^{-1} can be detected, which corresponds to the signal of a close-in Super-Earth planet.

Other spectrographs with precision down to 10 ms^{-1} are used in the search and follow-up of exoplanets, such as SOPHIE at the Observatoire de Haute Provence in France

---

[13]The habitable zone around a star is defined as the range in distance from the star where water can be in its liquid state

which is optimised for the search for exoplanets.

Figure 1.7 shows the planet detection limits for different instruments with different photometry and radial velocity precisions, and different lengths of survey.
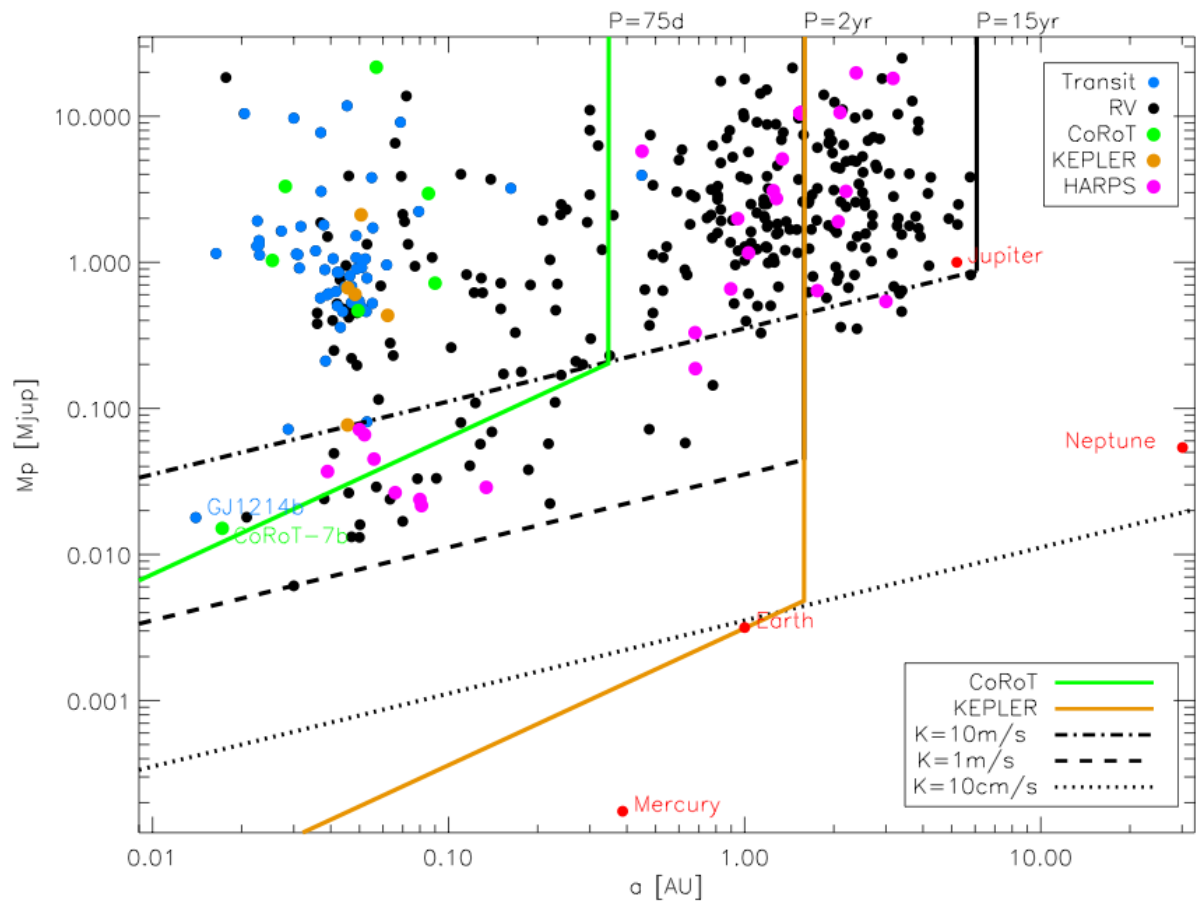

Figure 1.7: Diagram of the planet mass M_p versus orbital semi-major axis a of the exoplanets discovered by Jan 26th 2010 with the transit method (blue, green, and orange dots) and with the radial velocity method (black and pink dots). The diagonal black lines mark the detection limits in planet mass-separation for a planet around a ($M_\odot$, $R_\odot$) star using instruments with precision in radial velocity measurements of $10\,\mathrm{ms^{-1}}$(dashed-dotted line), $1\,\mathrm{ms^{-1}}$(dashed line), and $10\,\mathrm{cms^{-1}}$. The diagonal green and orange lines mark the detection limits in planet mass-separation for a planet around a ($M_\odot$, $R_\odot$) star using CoRoT and Kepler respectively. These lines are drawn for an observation of at least two transits with combined signal-to-noise ratio of 20, in a light curve with a photometric precision of 200ppm for CoRoT (Aigrain et al., 2009) and 10ppm for Kepler (Jenkins et al., 2010) – ppm = parts per million, 100ppm = 0.1 mmag. The vertical lines mark the upper limits in planet to star separations – detection of at least two orbital periods to secure the periodicity of the signal – due to the finite duration of the surveys: 30 years of radial velocity data (black), 4 years of continuous Kepler observations (orange), and 150 days of continuous CoRoT observations (green).

1.5.2   Future of the transiting exoplanet search and characterisation

The future of the characterisation of exoplanets lies with bigger telescopes, as a larger collecting area means more photons and thus a lower level of photon noise. The future instruments will also need to be more stable to reduce the level of correlated noise. For instance a more stable wavelength calibration for a spectrograph will allow the detection of fainter radial velocity variations. The future in the detection of Super-Earth atmospheres using the transit method lies in the new target choice of near-by (brighter) small host stars (larger planet-to-star radius ratio).

Near future: The JWST (James Webb Space Telescope), estimated to be launched in 2014, is a cooled infrared telescope with a segmented 6-m diameter mirror which will observe the transits of known exoplanets at various infrared wavelengths to study the atmosphere of Super-Earths orbiting small stars. The ground-based ELTs (Extremely large Telescopes), include the E-ELT (European-Extremely Large Telescope) 42-m telescope, the GMT (Giant Magellan Telescope) equivalent to a 25-m telescope, and the TMT (Thirty Meter Telescope), and will allow follow-up study from the ground of even more of the detected exoplanets (atmosphere, albedo, etc). The building stage of the E-ELT is estimated to start in 2010 for a start of operations planned for 2018. Future spectrographs, such as CODEX on the E-ELT, are being designed to reach precision down to $0.01\,\mathrm{ms}^{-1}$ which will allow the detection of radial velocity signals of Earth-like planets. To improve the precision in radial velocity measurements, new wavelength calibration techniques are needed and are being developed, such as the Laser Comb.

And after: The next generation of space mission searching for transiting exoplanets are being designed to look for the nearest transiting planets, targeting the bright stars (9th to 11th magnitude) across the whole sky. These missions include the PLATO mission (PLAnetary Transits and Oscillations of stars) and the TESS mission (Transiting Exoplanet Survey Satellite). They will use an array of small cameras with large fields of view and high resolution CCDs to monitor large areas of the sky. If funded, they should be launched from 2015 onwards. In a more distant future, proposed missions include TPF (Terrestrial Planet Finder) and Darwin, which are space missions with telescopes and/or instruments flying in formation in space. These missions are designed to study the light from the exoplanets themselves, using infrared nulling interferometry or visible-light coronography to suppress the light from the planet host star without affecting the light from the planet, therefore increasing the planet-to-star light ratio. If funded, these missions should be launched after 2020.

Foreseen challenges: For next generation telescopes and instruments, the challenges of studying small exoplanets which will limit the precision of their measurements include, physical processes such as the level of stellar activity for transits and radial velocities studies, and the level of dust emission for direct imaging. The solution to these limiting factors, if any, will most likely be in the development of new data processing and analysis techniques. From an instrumental point of view, the challenges are in

the improvement of the precision of the radial velocity measurements in the optical (for Earth-size planets around solar-type stars) and in the infrared (for Earth-size planets around M-dwarfs), and in the improvement of the nullifying techniques to better suppress the stellar light for the direct imaging of exoplanets.

1.6 This thesis

1.6.1 Motivations

The radius R_p and the mass M_p of an exoplanet can be ascertained when measuring both the flux and the radial velocity variations of the parent star due to its orbiting planetary companion. Improving the precision of observational planet masses and radii is important for both planet structure and planet formation models. The internal structure of a planet can be studied by comparing its mass and radius to model predictions of planets with different composition. Determining planet structure is important to derive observational statistics on planet types, which can then be compared to the predictions of planet formation models. Seager et al. (2007) show that to determine the composition of planets smaller than Uranus, error bars of less than 2% on the planet parameters are required. The current uncertainties on planet masses and radii are of order 10%. Improving these measurements is thus vital to help confirm the models.

As mentioned in Section 1.4.3, a side effect of the current photometric variability filters is that optimal stellar variability filtering, changes the shape of a transiting planet's light curve, and so the planet's properties derived from that light curve. As for small planets, the major source of uncertainty comes from the transit light curve, improving the processing of the light curve before deriving the planet parameters is essential. The first motivation of the thesis is thus to design a stellar variability filter that filters out the stellar variability whilst reconstructing the original transit signal as much as possible. This should enable us to derive more precise planet parameters from the transit light curve.

As seen in Section 1.4.4, the major contributor to the uncertainties of the planet parameters for large planets, are the precision of the stellar mass and radius which are derived from the stellar parameters inputed into the stellar evolution models. Thus, the second motivation of this thesis is to reduce the uncertainty of the stellar atmospheric parameters, starting with the stellar effective temperature which is used to derive the other parameters.

1.6.2 Structure

In Chapter 2, I present a new stellar variability filter, the Iterative Reconstruction Filter (IRF), and discuss its performance on simulated data. In Chapter 3, I re-derive the planet parameters of the first seven CoRoT planets using the IRF-filtered light curves. A by-product of the IRF is the reconstruction of all signals at the orbital period of the

planet. In Chapter 4, I search for secondary eclipses and orbital phase variations in the IRF-filtered light curves of CoRoT-1b and CoRoT-2b. In Chapter 5, I present a new temperature calibration to derive stellar effective temperatures using ratios of equivalent width of spectral lines, and re-derive the effective temperatures of the first nine CoRoT planet host stars. In Chapter 6, I combine the outcomes of the two new techniques presented in this thesis, i.e light curve filtering using the IRF and T_{eff} determination using calibrated equivalent width line ratios, by re-deriving the planet parameters of CoRoT-2b using a Markov Chain Monte Carlo (MCMC) on the IRF-filtered light curve. This approach takes into account the prior knowledge on the stellar temperature, taken as the equivalent width T_{eff} derived in Chapter 5. In Chapter 7, I summarise what has been discovered in this thesis (techniques developed, results, comparison with the literature and implication to the physics of the planets) and I finish with a few words on future prospects.